Depth Calibration and Validation of the Experimental Advanced Airborne Research Lidar, EAARL-B

Authors: Wright, C. Wayne, Kranenburg, Christine, Battista, Timothy A., and Parrish, Christopher

Source: Journal of Coastal Research, 76(sp1) : 4-17

Published By: Coastal Education and Research Foundation

URL: https://doi.org/10.2112/SI76-002

Journal of Coastal Research	SI	76	4–17	Coconut Creek, Florida	2016

Depth Calibration and Validation of the Experimental Advanced Airborne Research Lidar, EAARL-B

C. Wayne Wright[†], Christine Kranenburg[‡*], Timothy A. Battista[§], and Christopher Parrish[††]

[†]U.S. Geological Survey
Earth Resources Observation and Science Center
Sioux Falls, SD 57198, U.S.A.

[‡]CNTS/U.S. Geological Survey
St. Petersburg Coastal and Marine Science Center
St. Petersburg, FL 33701, U.S.A.

[§]National Oceanic and Atmospheric Administration
National Centers for Coastal Ocean Science
Silver Spring, MD 20910, U.S.A.

[††]Oregon State University
School of Civil and Construction Engineering
Corvallis, OR 97331, U.S.A.

www.cerf-jcr.org

www.JCRonline.org

ABSTRACT

Wright, C.W.; Kranenburg, C.; Battista, T.A., and Parrish, C., 2016. Depth calibration and validation of the Experimental Advanced Airborne Research Lidar, EAARL-B. *In*: Brock, J.C.; Gesch, D.B.; Parrish, C.E.; Rogers, J.N., and Wright, C.W. (eds.), *Advances in Topobathymetric Mapping, Models, and Applications*. *Journal of Coastal Research*, Special Issue, No. 76, pp. 4–17. Coconut Creek (Florida), ISSN 0749-0208.

The original National Aeronautics and Space Administration (NASA) Experimental Advanced Airborne Research Lidar (EAARL), was extensively modified to increase the spatial sampling density and improve performance in water ranging from 3–44 m. The new (EAARL-B) sensor features a 300% increase in spatial density, which was achieved by optically splitting each laser pulse into 3 pulses spatially separated by 1.6 m along the flight track and 2.0 m across-track on the water surface when flown at a nominal altitude of 300 m. Improved depth capability was achieved by increasing the total peak laser power by a factor of 10, and incorporating a new "deep-water" receiver, optimized to exclusively receive refracted and scattered light from deeper water (15–44 m). Two clear-water missions were conducted to determine the EAARL-B depth calibration coefficients. The calibration mission was conducted over the U.S. Navy's South Florida Testing Facility (SFTF), an established lidar calibration range located in the coastal waters southeast of Fort Lauderdale, Florida. A second mission was conducted over Lang Bank, St. Croix, U.S. Virgin Islands. The EAARL-B survey was spatially and temporally coincident with multibeam sonar surveys conducted by the National Oceanic and Atmospheric Administration (NOAA) ship *Nancy Foster*. The NOAA depth data range from 10–100 m, whereas the EAARL-B captured data from 0–41 m. Coefficients derived from the SFTF calibration mission were used to correct the EAARL-B data from both missions. The resulting calibrated EAARL-B data were then compared with the original reference dataset, a jet-ski-based single beam sonar dataset from the SFTF site, and the deeper NOAA data from St. Croix. Additionally, EAARL-B depth accuracy was evaluated by comparing the depth results to International Hydrographic Organization (IHO) standards. Results show good agreement between the calibrated EAARL-B data and all three reference datasets, with 95% confidence levels well within the maximum allowable total vertical uncertainty for IHO Order 1 surveys.

ADDITIONAL INDEX WORDS: *Bathymetry, laser hydrography*.

INTRODUCTION

Airborne bathymetric lidar is an important capability for supporting navigational safety and charting, but increasingly, also a valuable tool for evaluating ecosystem services and coastal marine planning. While most hydrographic surveys are conducted from launches or oceanographic vessels using multibeam echosounders (MBES), nearshore shallow-water (< 15 m) ship-based acquisition is time intensive and navigationally challenging. Hydrographic surveys are particularly challenging in tropical marine waters where fringing reef and exposed or semi-submerged rock outcrops can preclude data collection. In addition, tropical marine locations are particularly conducive for airborne lidar collection given desirable water quality conditions optimum for laser penetration to the seafloor.

Understanding the seafloor topography, habitat composition, and habitat condition is of critical importance in coastal waters to inform and support conservation, management, and research activities. Bathymetric lidar provides a fundamental spatial dataset to support subsequent investigations, such as living marine resource distribution, abundance, and biogeographical linkages; evaluating instantaneous and time series impacts of natural and anthropogenic stressors; considering regulatory or coastal development situations; and supporting resiliency and restoration efforts. The need for spatial information is typically amplified within nearshore waters, where traditionally there has been a paucity of data. Airborne lidar and, in particular, the Experimental Advanced Airborne Research Lidar, version B (EAARL-B), which is one of the few sensors to have a broad enough depth range to be truly useful across the seascape, provides the capability to satisfy the desired data requirement.

DOI: 10.2112/SI76-002 received 12 June 2015; accepted in revision 7 January 2016.
*Corresponding author: ckranenburg@usgs.gov

The EAARL-B Sensor

Recent enhancements to the EAARL greatly improved the system's ability to collect topobathymetric data. The original system (Wright and Brock, 2002) had a maximum depth ability of 27 m and only one spatial channel, optimized for shallow water. The new enhanced version has a maximum demonstrated depth capability of 44 m and four spatial channels, three which are optimized for shallow water and one optimized for deep water.

The original EAARL system illuminated a single point on the surface for each laser pulse. In the EAARL-B, each laser pulse is optically divided into three pulses that travel to the surface at the same time and that are nearly parallel. The three illuminated points on the land/water surface are nominally spaced 1.6 m apart along the flight track and 2.0 m apart across-track, when flown at a nominal altitude of 300 m. Sample spacing can be optionally increased to 1 m across-track. From the nominal operating altitude of 300 m, each illuminated spot is approximately 30 cm in diameter and each spot has a corresponding, co-located coaxial receiver pixel, which is approximately 60 cm in diameter. A fourth, much larger, receiver pixel encompasses all three illuminated spots. This receiver pixel is approximately 5 m in diameter at the water surface (Figure 1).

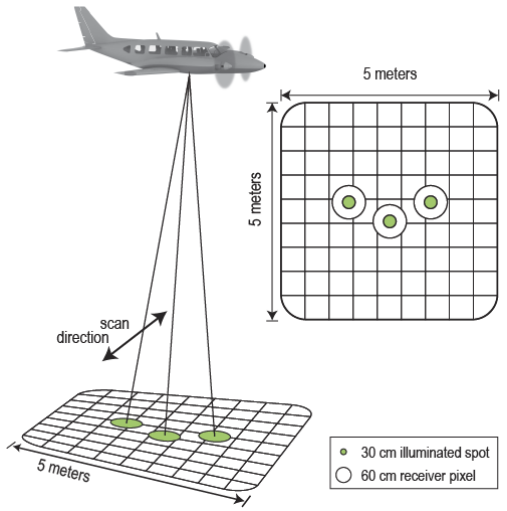

Figure 1. Footprint of the EAARL-B receiver showing relative size and positions of topobathy-channel fields of view (circles) to deep-channel collection area. Hatched area represents the deep-channel field of view.

Each laser pulse is divided into three spatially separated beams for two reasons: 1) to reduce the energy density below American National Standards Institute (ANSI) eye safe limits, and 2) to increase the spatial point density by a factor of three. The three beams, hereinafter referred to as the shallow or topobathy channels, are effective for subaerial topographic mapping and for submerged topographic mapping in optically shallow water, ranging from zero to approximately 20 m depth. Beyond 20 m, the three beams are sufficiently refracted by surface waves and scattered by suspended particles in the water column such that little energy remains within their coaxial receiver pixels. The laser energy that is refracted and scattered is not necessarily absorbed and lost; however, acquiring depth data beyond 20 m necessitated the development of an additional deep-water channel. If the laser energy at these depths is within the field of view of the large 5-m diameter "deep-channel pixel," this energy can be detected.

The laser light pulse travels approximately 29.971 cm per nanosecond in air, and 22.490 cm per nanosecond in water. Since the light must travel from the aircraft to the surface(s) and back again in order to be detected, those distances are divided in half, giving 14.985 cm per nanosecond in air and 11.245 cm in water. The refractive index of air is ~1.000276 and of water is ~1.333, although both vary slightly in response to a number of variables.

It is critically important that a reflected return signal be received from the surface of the water so the change in the speed of light between the air and water can be correctly accounted for. There are two distinct mechanisms that can produce a signal from the surface region. The first is the reflection from the discontinuity in dielectric between air and water, and the second is largely from suspended particulate material at or near the surface. There is an important difference in how these two mechanisms reflect light. The first produces a highly specular reflection, where the angle of reflection, with respect to the surface normal, is equal to, but opposite from, the angle of incidence. This surface reflection varies strongly as a function of lidar scan angle and surface sea state. The second mechanism is non-specular; however, its strength depends on suspended particulate matter in the water column. While particulate matter helps give a good signal at or near the surface, the presence of particulates will limit the depth measurement capability of the lidar. Additionally, suspended sediment tends to spread the returned laser pulse, making it difficult to use for determining the exact location of the surface (Guenther, LaRocque, and Lillycrop, 1994).

Each channel of the EAARL-B uses a photomultiplier tube (PMT) to detect the incoming reflected laser light. A PMT is an extremely fast photodetector, characterized by its transit time and transit time spread (TTS), where the transit time is the time delay between the arrival of a light pulse at the PMT and appearance of the amplified electrical output pulse, and the TTS is a measure of transit time variability (Hamamatsu Photonics K.K., 2007). The three topobathy channels use identical PMTs with a photo-electron transit time of 5,400 picoseconds and a TTS of 230 picoseconds, whereas the deep channel uses a different, more sensitive and higher gain photomultiplier with a photo-electron transit time of 2,700 picoseconds and an electron TTS of 200 picoseconds. These transit time spreads correspond to an uncertainty of 3.4 cm in slant range measurement in air and 2.5 cm in water for the topobathy channels and 2.95 cm in air and 2.2 cm in water for the deep channel. These values establish the absolute lower limit of ranging uncertainty of the EAARL-B.

Table 1. *International Hydrographic Organization minimum standards for hydrographic surveys.*

Order	Description	Max. Allowable Total Horizontal Uncertainty (m)	Parameter a of Max. Total Vertical Uncertainty (m)	Parameter b of Max. Total Vertical Uncertainty
Special Order	Areas where under-keel clearance is critical	2	0.25	0.0075
Order 1	Areas shallower than 100 m and where under-keel clearance is less critical but features of concern to surface shipping may exist	5 + 5% of depth	0.5	0.013

Raster versus Conical or Circular Scanning

The EAARL-B uses a raster scanner more typical of topographic lidars. Most bathymetric lidars use a conical, circular, or semi-circular scan pattern for two primary reasons: (1) it yields a relatively constant and substantial off-nadir angle of incidence to the water surface, and (2) it helps reduce the dynamic range of the water-surface Fresnel reflection, which in turn reduces the dynamic performance requirements of the receiver channel(s). One important disadvantage of conical and circular scanning is the constant high angle of incidence, which leads to high geometric pulse spreading. It occurs because most bathymetric lidars use a beam divergence of several milliradians to illuminate relatively large (~2 m) spots on the surface of the water, which increases the geometric surface-regime pulse stretching and decreases the accuracy of the surface-return elevation measurement (Guenther, 1985). It is currently impractical or even impossible to know from what portion of the stretched, illuminated spot the reflected energy is returned.

The EAARL-B raster scan has a nominal off-nadir pitch value of 2.3 degrees to avoid nadir surface Fresnel reflections. The system must demonstrate that it is capable of accurate submerged-topography measurement over a wide range of laser angles of incidences, and in the presence of strong surface-return reflections since it scans over a much larger range of scan angles than circular or conical scanners. One advantage of the raster scan is a more uniform distribution of surface points at a given laser pulse rate. Another advantage is that a significant number of points are collected near nadir, where the propagated uncertainty in lidar point coordinates, due to pitch and roll uncertainty, reaches a minimum (Baltsavias, 1999). Conical and circular scanners result in increased propagated uncertainty in lidar point coordinates from roll and pitch uncertainty due to the large, nominally constant, off-nadir angle. The EAARL-B varies its pulse rate as a function of the scan angle to enhance surface-sample distribution.

Position and Orientation-introduced Errors

Uncertainties in the post-processed, blended navigation solution from the global navigation satellite system (GNSS)-aided inertial navigation system (INS) comprise a major component of the propagated uncertainty in three-dimensional spatial coordinates of lidar points. Component uncertainties in GNSS are attributable to multipath, ionosphere, satellite orbits, satellite clocks, troposphere, and receiver noise (Grewal, Andrews, and Bartone, 2013). These component uncertainties can be reduced in post-processed kinematic GNSS software through the use of survey-grade, multi-frequency receivers, survey-grade aircraft antennas, short baselines, and precise ephemerides. Uncertainty in navigation data obtained with an INS is largely a factor of gyro and accelerometer drift. Integration with a Kalman filter enables the complementary error characteristics of GNSS and INS to be leveraged to reduce uncertainties in the blended navigation solution, with tightly coupled implementations often being advantageous in kinematic surveying (Grewal, Andrews, and Bartone, 2013; Hutton *et al.*, 2008).

Additional component uncertainties in airborne lidar include range-measurement uncertainty, and scan angle uncertainty. For bathymetric measurement, additional uncertainty comes from the detection of the water surface (Guenther, LaRocque, and Lillycrop, 1994; Guenther, Thomas, and LaRocque, 1996). In this study, the spatial accuracy of an EAARL-B lidar point is assessed empirically through comparison against independent, "reference" datasets of higher accuracy, expressed at the 95% confidence level, and examined in relation to maximum permissible total vertical uncertainty (TVU) and total horizontal uncertainty (THU), as specified for different hydrographic survey orders in IHO S-44-5E (International Hydrographic Organization, 2008).

The IHO Standard

The EAARL-B was not designed with the intent of meeting the IHO S-44-5E Minimum Standards for Hydrographic Surveys (International Hydrographic Organization, 2008). However, the depth measurement uncertainty criteria for IHO Special Order and Order 1 surveys provide a convenient means for assessing and describing the results of the EAARL-B performance evaluation.

While the IHO standards also include requirements for bottom-feature detection, full seafloor search, and horizontal-accuracy requirements, this work focuses exclusively on IHO vertical depth requirements. The IHO vertical depth criteria are well established reference standards that are employed for evaluating EAARL-B depth-accuracy performance. The IHO defines the TVU as the vertical component of the total propagated uncertainty. Total propagated uncertainty includes both random and systematic measurement error as well as error introduced from derived or calculated parameters. TVU is computed as follows:

$$TVU = \pm\sqrt{a^2 + (bd)^2} \quad (1)$$

where a represents that portion of the uncertainty that does not vary with depth, b is a coefficient that represents the portion of the uncertainty that varies as a function of depth, and d is depth;

therefore, *bd* is the portion of the uncertainty that varies with depth.

The IHO S-44-5E specifies the uncertainty at the 95% confidence level, assuming a normal Gaussian distribution, and one-dimensional (1D) quantity (depth only). The IHO S-44-5E defines the 95% confidence level in the 1D case as 1.96 times the standard deviation. Using Equation 1 and the coefficients specified in Table 1, maximum TVU values have been computed for the depth range covered by the EAARL-B system (Table 2).

Table 2. *Total Vertical Uncertainty values for various depths*.

Depth (m)	Special Order (m)	Order 1 (m)
5	0.25	0.50
10	0.26	0.52
15	0.27	0.54
20	0.29	0.56
25	0.31	0.60
30	0.34	0.63
35	0.36	0.68
40	0.39	0.72

Reference Datasets

EAARL-B bathymetric data were compared with three different reference datasets in two different geographic locations. The calibration and primary dataset consisted of a lidar dataset collected 9 years earlier at the SFTF site southeast of the Ft. Lauderdale International Airport (FLL) and ranges in depth from near zero to 40 m. The second was a multibeam sonar dataset collected concurrently with EAARL-B data in St. Croix, U.S. Virgin Islands (STX) and ranges in depth from 10 to 100 m. The final dataset was single beam sonar collected by jet ski within a few days of the EAARL-B survey. There were no unsettling weather events between the jet ski survey and the EAARL-B survey. The jet ski data covered a depth range from 0.9 to 35 m; however, only depths between 0.9 and 10 m were determined to be usable for validation.

The JALBTCX Primary Reference Dataset

The JALBTCX bathymetric lidar reference dataset collected at the SFTF site was selected for the calibration. The U.S. Army Corps of Engineers (USACE) collected the reference dataset in 2005 using their Optech SHOALS-3000 3 kHz lidar (Irish and Lillycrop, 1999; Long, Cottin, and Collin, 2007), which uses a hemispherical constant angle-of-incidence scan pattern. The USACE cross-calibrated and validated the reference dataset against multibeam and other measurements from the SFTF before providing it to the USGS. Although the reference dataset was 9 years old at the time of the calibration flights, the bottom topography appears to be stable where there is hardbottom. The USACE provided the reference dataset to the USGS in the North American Datum of 1983 (NAD83) epoch 2010.00 coordinate system as a laser file format (LAS) point-cloud dataset.

The JALBTCX reference dataset was processed in ITRF-2005 and converted to NAD83 (2011) using the NOAA National Geodetic Survey's (NGS) VDatum tool (Hess, Jeong, and White, 2013; NOAA 2012). The data are the result of more than a dozen flights between June 23, 2005, and July 6, 2005, covering 56 km^2 and 51 million samples with greater than 200% coverage of more than 85% of the entire test area. The data were used to produce a 2-m mean depth surface for validating Coastal Zone Mapping and Imaging Lidar (CZMIL) sensors.

Sandy areas were readily apparent and easily discernible by visual inspection of the bathymetric digital elevation map (DEM) when analyzing the difference between the reference and the EAARL-B data, and were not used for EAARL-B calibration. The unstable sandy areas appeared to be limited to depths shallower than 6.5 m along the beach. One of the primary reasons for selecting the SFTF site is the clarity of the water. This area features near-optimal water properties, that is, clear water, relatively free of suspended sediment and dissolved organic material. This enables the EAARL-B to receive bottom-return signals that cover as much as possible of its operational depth range of 0 to 44 m. During the survey, the EAARL-B was able to capture data between 0 and 34 m depth.

The NOAA Multibeam Sonar Dataset

The second reference dataset consists of multibeam sonar data collected by NOAA National Centers for Coastal Ocean Science between March 12 and April 2, 2014, over Lang Bank, St. Croix, U.S. Virgin Islands, coincident with EAARL-B surveys. The NOAA ship *Nancy Foster* conducted the hydrographic survey using a Reson SeaBat 7125-SV2 dual frequency sonar capable of operating at 200 or 400 kHz and an integrated Reson SVP 71 sound velocity sensor. The 7125-SV2 multibeam is mounted on the hull and is located port of the keel and forward of the reference point of the vessel. The 7125-SV2 was operated at 400 kHz for the duration of the cruise. The 7125-SV2 produced a 128-degree swath of 512 equiangular beams with an along-track beam width of 1.1 degrees and across-track beam width of 0.5 degree. A multibeam patch test was performed for the Reson 7125-SV2 sonar system on March 21, 2014 (DN080), to calibrate the sonar system, and a total vertical uncertainty quality check (TVU QC) was performed to ensure that data acquired met the required IHO Order 1 specifications (Battista and Stecher, 2014). The dataset was delivered referenced to the NAD83 (2011) datum, with depths relative to the NOAA chart datum, Mean Lower Low Water (MLLW).

The USGS Single Beam Sonar Dataset

The third reference dataset consists of single beam sonar data collected at the SFTF site by the USGS within 1 day of the EAARL-B surveys. The near-concurrent jet ski data were used to evaluate the EAARL-B performance over the depth range from 0.9 to 10 m. The more recent jet ski data were desired because the primary reference dataset was 9 years old, and the areas shallower than 6.5 m are dominated by shifting sand. The data were collected using two jet-ski-mounted System for Accurate Nearshore Depth Surveying (SANDS) systems (Hansen, 2008) along two lines perpendicular to and extending 1.75 km from the beach. Data were collected along each line on

both the outbound and inbound journeys, and a diagonal line, which intersected the offshore lines, was then run in order to check the consistency of depth measurements at intersection points. The dataset was delivered referenced to the World Geodetic System 1984 (WGS84), realization G1674, and contained ellipsoid heights. While the jet ski data were collected over the depth range from zero to 35 m, the accuracy was degraded in the deeper portions because the jet skis are not equipped with attitude and orientation systems. Pitch and roll due to sea state causes a substantial angle between the slant range and the vertical water depth. The resulting uncorrectable measurement error becomes too large to be useful in water deeper than about 10 m.

The Central Questions

This study examines the following central questions:

(1) What are the depth (range) calibration constants for each of the EAARL-B channels?
(2) Do the shallow channels and the deep-channel track each other, or do they need separate depth calibration?
(3) Do the three independent surface spots combine in the deep channel in a way that produces a reliable accurate depth measurement?
(4) How do the deep-channel measurements statistically compare with the shallow channels and what is the relationship?
(5) Is the relationship reliable?
(6) Are the EAARL-B depth data in agreement with the reference data, and if not, what is the relationship (*e.g.*, linear, nonlinear, constant, *etc*.)?

METHODS

Depth calibration of the EAARL-B involves four steps: (1) runway calibration of the topobathy channels, (2) alignment of the deep channel to the topobathy channels, (3) derivation of the depth calibration coefficients, and (4) testing the coefficients by applying them to different EAARL-B surveys at multiple locations covering the entire operational depth range of the sensor.

Subaerial Calibration

Before attempting to calibrate the EAARL-B for depth, it was first calibrated using a ground-based topographic dataset of the runway complex at the Salisbury Wicomico Ocean City Airport in Salisbury, Maryland. The runway ground-survey data were collected in November 2008 using two Ashtech Z-EuroCard Global Positioning System (GPS) dual-frequency survey receivers and Ashtech choke ring antennas, model 701945-01, rigidly mounted to a wheeled cart towed behind a vehicle. The data from the ground survey were processed to point data in the WGS84 (G1150) coordinate reference system.

The EAARL-B was flown over each of the two runways in opposing directions and the resulting EAARL-B point-cloud points were matched with the ground-survey point cloud and the differences determined. This process was repeated 10 more times over a period of 2 years, resulting in an average mean error of 2.8 cm and an average standard deviation between the EAARL-B points and the ground survey of 4.8 cm. The eleven runway calibration flights were conducted between August 1, 2012, and September 18, 2014. Figure 2 shows the mean error between each calibration flight and the runway ground survey.

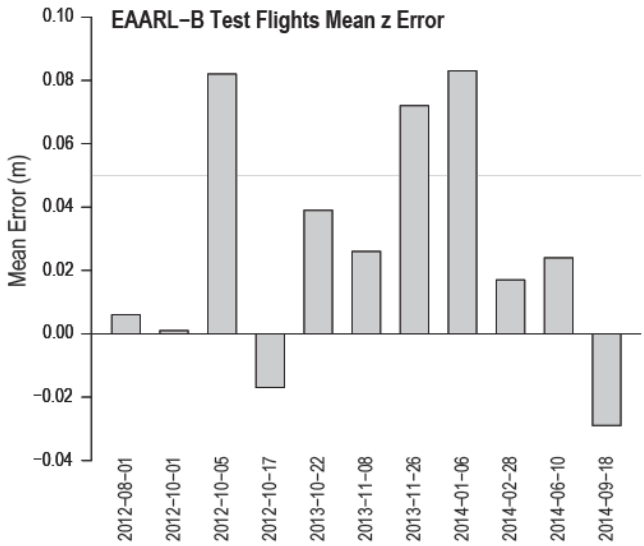

Figure 2. Difference between successive EAARL-B calibration flights and the runway ground survey.

Shallow-water Calibration of the Deep Channel

The EAARL-B deep channel cannot be accurately calibrated using traditional ground calibration or subaerial overflight because the deep-channel receiver does not contain the actual illuminated surface spots within its field of view (Figure 1) and also because it relies on scattered light from a meter or more of water column to produce a suitable bottom-return signal. This required scattering and refraction does not occur sufficiently in the air or from subaerial (land) targets. The only acceptable method of calibrating this channel is by overflight of a suitable test site covering a substantial portion of the total range of operational depths.

Calibration of the deep channel leverages the simple idea that depth measurements returned by both deep and shallow channels should be the same for any flat area for which they both detect a bottom; specifically, a vertical offset is determined which minimizes the difference in the mean error between topobathy-channel depths and deep-channel depths. Figure 3a shows the effects of channel misalignment; Figure 3b shows the same error distributions after the deep channel was reprocessed with a new offset. Any event that disturbs the relative positions of the optical components, for example cleaning the mirrors, will necessitate realignment of the deep channel. To determine the value of the range bias required to bring them into alignment, the means of the kernel density estimate curves of deep-channel errors were aligned with the corresponding means of the kernel density estimate curves of topobathy-channel errors.

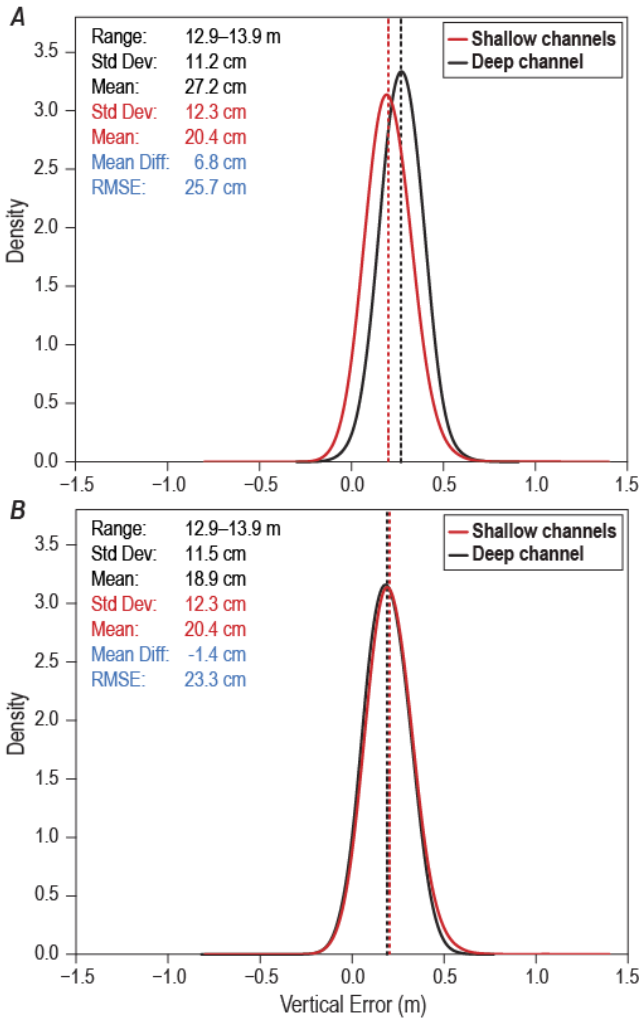

Figure 3. Density estimates and statistics of vertical error (A) before and (B) after channel alignment for polygon G in SFTF. Red distributions are from the EAARL-B topobathy channels, and black distributions are the deep channel. Plots are based on uncalibrated data.

Calibration Mission Flights

Two calibration-survey flights were flown on April 21 and April 22, 2014. The EAARL-B survey aircraft operated from the Albert Whitted (KSPG) airport located in St. Petersburg, Florida, and transited to and from the FLL/SFTF survey area, without landing, on both survey days. While in the survey area, the ZMA1 Continuously Operating Reference Station (CORS) GPS station was used as the kinematic base station. ZMA1 is nominally 25 km southwest of the calibration site and provides 1 Hz dual-frequency GPS data. The EAARL-B GPS data were processed using precision GPS ephemeral data in the Novatel Inertial Explorer software program, referenced to the NAD 83 coordinate system. The aircraft was flown at a nominal altitude of 1,100 feet (~335 m) on parallel and zigzag flight lines along the coastline and within the JALBTCX site polygon.

Selection of Calibration Regions

The objective of this study was to calibrate the depth measurements made by the EAARL-B and not to conduct an overall accuracy assessment of lidar performance in terms of horizontal accuracy, or accuracy where there is substantial topographic relief, slope, or complex small-scale bottom structure. To facilitate optimal conditions for determining vertical error and depth-dependent offsets, the data were analyzed and polygons were delineated at 23 distinct depth ranges from 6.3 to 34 m. Each polygon was examined and analyzed for average depth, roughness, topographic complexity, levelness, flatness, and for overlap between the JALBTCX and EAARL-B surveys. Figure 4 shows the selected comparison regions. References to named polygons throughout this paper correspond to those defined in this figure.

Areas with minimal sand were selected. Additionally, areas with spur-and-groove reefs, coral rubble, seagrass, and other complex small-scale bottom topography could erroneously influence the depth-calibration measurements or cause range noise in either the EAARL-B or the JALBTCX reference dataset, so those areas were avoided. Although there are plenty of data from both sensors between 0 and 6.5 m, all appeared to be sandy bottom and exhibited evidence of substantial geomorphologic change, so those areas were excluded from the calibrations.

Data Processing, Filtering, and Editing

The three small field of view channels measure topography and shallow-water bathymetry. Different processing algorithms are used for subaerial topography and bathymetry. In fact, there are two different algorithms for processing shallow bathymetry depending on the depth regime being processed. The same algorithm that is used to process deeper bathymetry from the three shallow channels is used with different parameters to process bathymetry from the deep channel.

Processing Software

The Airborne Lidar Processing System (ALPS) (Bonisteel *et al.*, 2009) was used to process the EAARL-B data. The bathymetric processing code (current as of ALPS codebase 2014-07-15, revision 9631aa56c46e) was used to process both the topobathy channels and the deep channel. The bathymetric control parameters were optimized to reduce noise and maximize bottom detection.

The depth-detection algorithm subtracts a user-defined normalized water-column model from each raw waveform. The model can be either a combination of exponential decays representing the laser and the water, or a fitted normalized log-normal function. Once the water-column effects are removed, potential bottom peaks are compared to a user-defined threshold and then further analyzed for expected bottom return pulse characteristics including pulse width, rise, and fall times. A higher threshold eliminates more noise, but also excludes deeper and/or weaker bottom signals. If the bottom return passes all the criteria set forth in the parameter file, it is accepted and returned as a valid bottom signal.

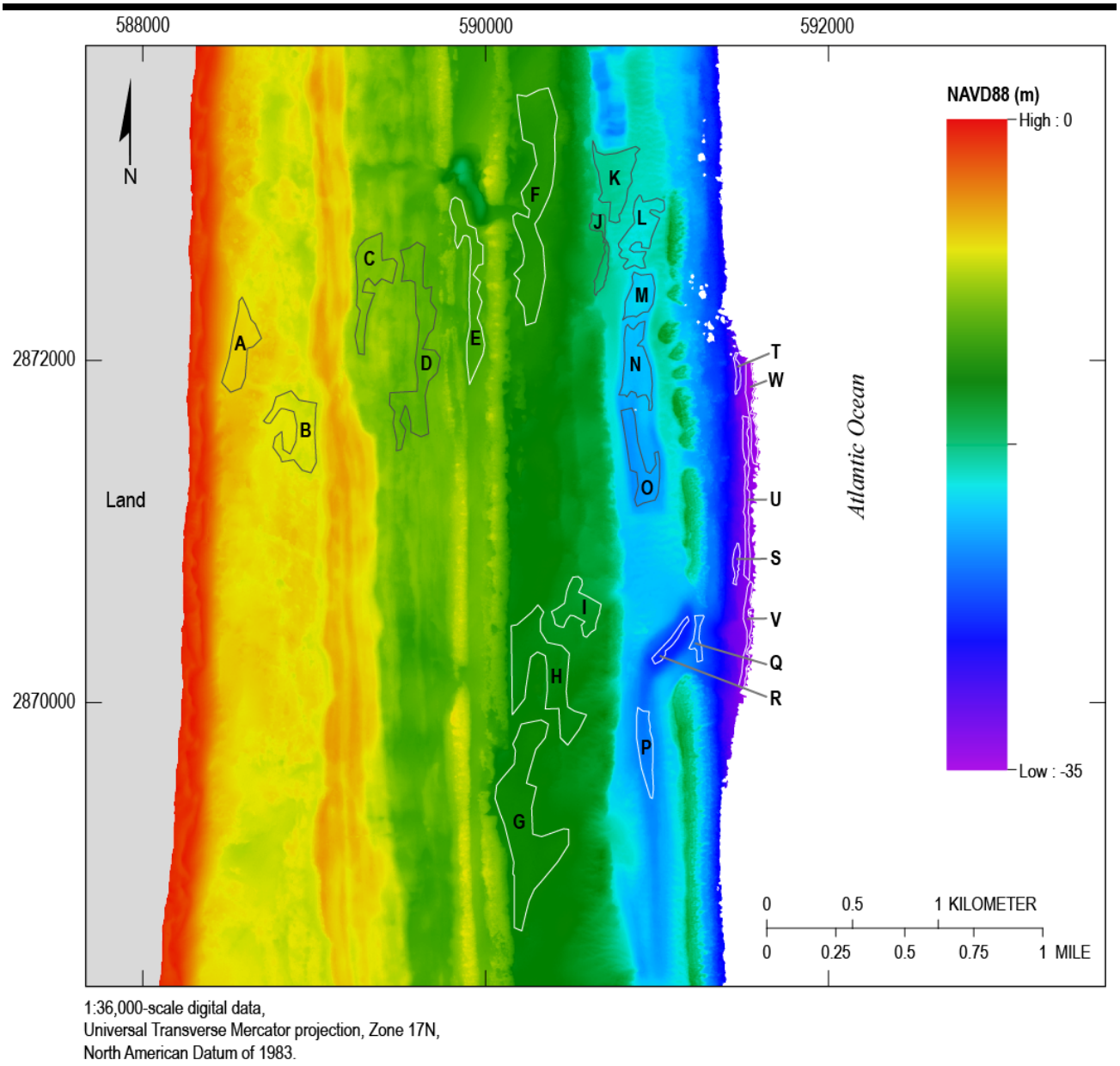

Figure 4. Polygons A–W define areas at selected depth regimes that are relatively flat, level, and free of sand, seagrass, and small-scale bottom structure that would introduce elevation errors. References to named polygons throughout this paper correspond to the areas defined here. (Elevations are referenced to the North American Vertical Datum of 1988.)

Figure 5a illustrates the components of the topobathy-channel bottom detection algorithm where the black line is a single raw EAARL-B waveform, the red line is the exponential decay model, and the blue line is the EAARL-B (adjusted) waveform after the water-column effects have been removed. The green line is the user-defined threshold, which a peak in the blue curve must exceed in order to be classified as a bottom return. Figure 5b illustrates the components of the deep-channel bottom detection algorithm. The line descriptions are the same as those of Figure 5a, except the decay model is a log-normal curve instead of an exponential curve.

Random Consensus Filtering

The built-in ALPS multi-gridded Random Consensus Filter (RCF) (Nagle and Wright, 2016) was used to automatically remove outliers and noise in both the topobathy and deep-

channel data. The RCF algorithm works by detecting where the highest concentration of points in each volume is located. These points are deemed a "consensus," and any points within the volume but outside a user-defined buffer distance from the consensus points are removed from the dataset. The number of points required to form a consensus, the dimensions of the volume, the maximum buffer distance, and the percent overlap are all user-defined parameters of the filter. For this dataset, the filter was set for a horizontal buffering cell size of 10 m, 1-m vertical, a 75% overlap with adjoining RCF cells, and a minimum of 3 points needed for consensus. The RCF function does not alter data points in any way except to either keep or reject them.

Manual Edits

The RCF function is effective at removing obvious water-column and random solar-radiation noise, but dense, highly correlated noise can pass the filter because the noise itself forms a consensus. Such noise is subsequently removed by manual inspection and editing.

Point-to-Point Comparison and Difference

The filtered and manually edited data were processed to find the nearest reference data points within 1-m horizontal. For each EAARL-B point within a designated polygon, the elevation difference between the EAARL-B point and the mean of the reference points within the 1-m circle was computed, and the mean and standard deviation were calculated on the resulting differences. The mean difference of a polygon is defined by Equation 2. This process was repeated for each of the selected depth polygons defined in Figure 4. The resulting statistics are tabulated in Table 3 and depicted graphically in Figure 6.

$$\text{Mean difference} = \frac{1}{N}\sum_{i=1}^{N}\left(\frac{\sum_{j=1}^{n} z_j}{n}\right) - z_i \qquad (2)$$

where n is the number of reference dataset points in a 1-m circle around an EAARL-B data point, z_j is the elevation of a reference dataset point, z_i is the elevation of an EAARL-B data point, and N is the number of EAARL-B points in the polygon.

Derivation of the Calibration Constants

Only the JALBTCX reference dataset was used in the derivation of the calibration constants. Kernel Density Estimation (Silverman, 1986) was used to smooth the vertical error distributions of each selected depth polygon. Figure 6 shows a scatterplot of the raw EAARL-B depth versus the combined mean difference of all four channels for each polygon defined in Figure 4. A simple linear regression analysis was performed on these data yielding slope and intercept coefficients of 0.98103 and –0.00068, respectively. The blue line in Figure 6 is the least squares fit. For a given EAARL-B raw depth, a corrected depth is computed by

$$y = m\,D_{eb} + b \qquad (3)$$

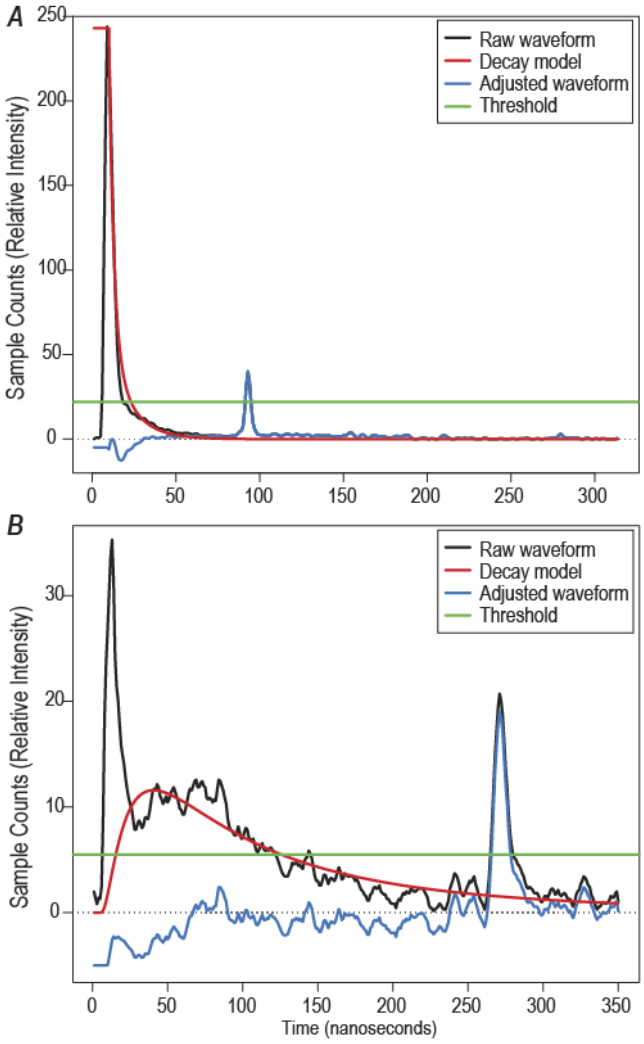

Figure 5. Components of the bathy processing algorithm for (A) shallow water, using an exponential decay model, and (B) deep water, using a log-normal decay model. The black line is a raw EAARL-B waveform, the red line is the decay model, the blue line is the EAARL-B waveform with water-column effects removed, and the green line is the threshold.

where the slope, m, equals 0.98103, the intercept, b, in meters, equals -0.00068, D_{eb} is the EAARL-B depth measurement, and y is the corrected depth.

Testing the Calibration Constants

In order to test the validity of the calibration constants, they were applied to both the SFTF and STX EAARL-B surveys, and the same procedure of defining test regions and calculating mean differences was performed. The calibration regions for the

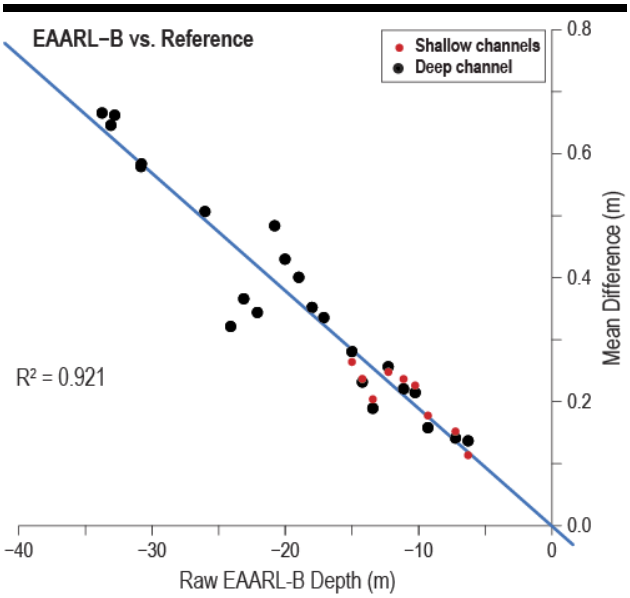

Figure 6. Scatterplot relating raw EAARL-B depths to reference dataset mean differences from which calibration coefficients are derived. Data points are mean differences between uncalibrated EAARL-B depths and the JALBTCX reference dataset. Black dots represent the deep channel; red dots represent the shallow (topobathy) channels.

SFTF survey were reused, and 30 regions with approximately 1-m (vertical) depth difference were selected for the St. Croix (STX) dataset within areas common to both the EAARL-B and NOAA MBES datasets. The polygons were selected to minimize depth variation and to exclude coral heads and other bottom topography that could contaminate the results by allowing small horizontal errors to be inappropriately translated into vertical errors. The selected polygons for STX are shown in Figure 7.

RESULTS AND DISCUSSION

The primary results of this study are the calibration coefficients needed to depth correct EAARL-B data collected in water with a diffuse attenuation coefficient value (K_d) on the order of 0.1. The results may be different for other water bodies with a higher K_d value.

Derivation of the Calibration Constants

Table 3 summarizes the statistics for each named depth polygon defined in Figure 4. The standard deviation is expected to increase with depth because beam spreading on the seafloor increases with depth. However, polygon A at 6.3-m depth has a higher standard deviation for the topobathy channels (13 cm) and deep channel (12.2 cm) relative to other regions in the 6- to 15-m range. This difference was caused by sand migration within the polygon that occurred during the 9-year interval between the JALBTCX survey and the EAARL-B survey. The topobathy channels demonstrated good laser penetration to 15-m depth, and strong statistical agreement (mean and standard deviation) with the deep channel.

Table 3. *Statistics of pre-calibration vertical error, per region, at the SFTF site.*

Poly	Average Reference Depth (m)	Topobathy Channels		Deep Channel	
		Mean (cm)	St. Dev (cm)	Mean (cm)	St. Dev (cm)
A	6.3	11.4	13.0	13.7	12.2
B	7.2	15.2	9.3	14.1	8.2
C	9.3	17.8	9.8	15.8	8.0
D	10.3	22.6	11.9	21.5	9.2
E	11.1	23.6	9.7	22.0	8.4
F	12.3	24.8	10.6	25.6	9.9
G	13.4	20.4	12.3	18.9	11.5
H	14.2	23.7	11.2	23.2	10.2
I	15.0	26.4	11.1	28.1	9.9
J	17.1	-	-	33.6	10.7
K	18.0	-	-	35.2	12.8
L	19.0	-	-	40.1	14.1
M	20.0	-	-	43.0	13.7
N	20.8	-	-	48.4	16.0
O	22.1	-	-	34.4	16.9
P	23.1	-	-	36.6	19.7
Q	24.1	-	-	32.1	24.1
R	26.0	-	-	50.7	20.6
S	30.8	-	-	58.4	18.7
T	30.8	-	-	57.9	16.0
U	32.8	-	-	66.2	21.7
V	33.1	-	-	64.6	27.4
W	33.8	-	-	66.6	27.3

Polygon names A–W correspond to named polygons in Figure 4.

Applying the Calibration Results

After deriving the calibration constants, they were applied to the entire SFTF dataset and the same selected depth polygons were reexamined. Validation of the constants was performed by comparing the calibrated EAARL-B data to the single beam jet ski data at SFTF and the NOAA MBES data at STX, the latter having been collected a month earlier, at a location more than 1,600 km away.

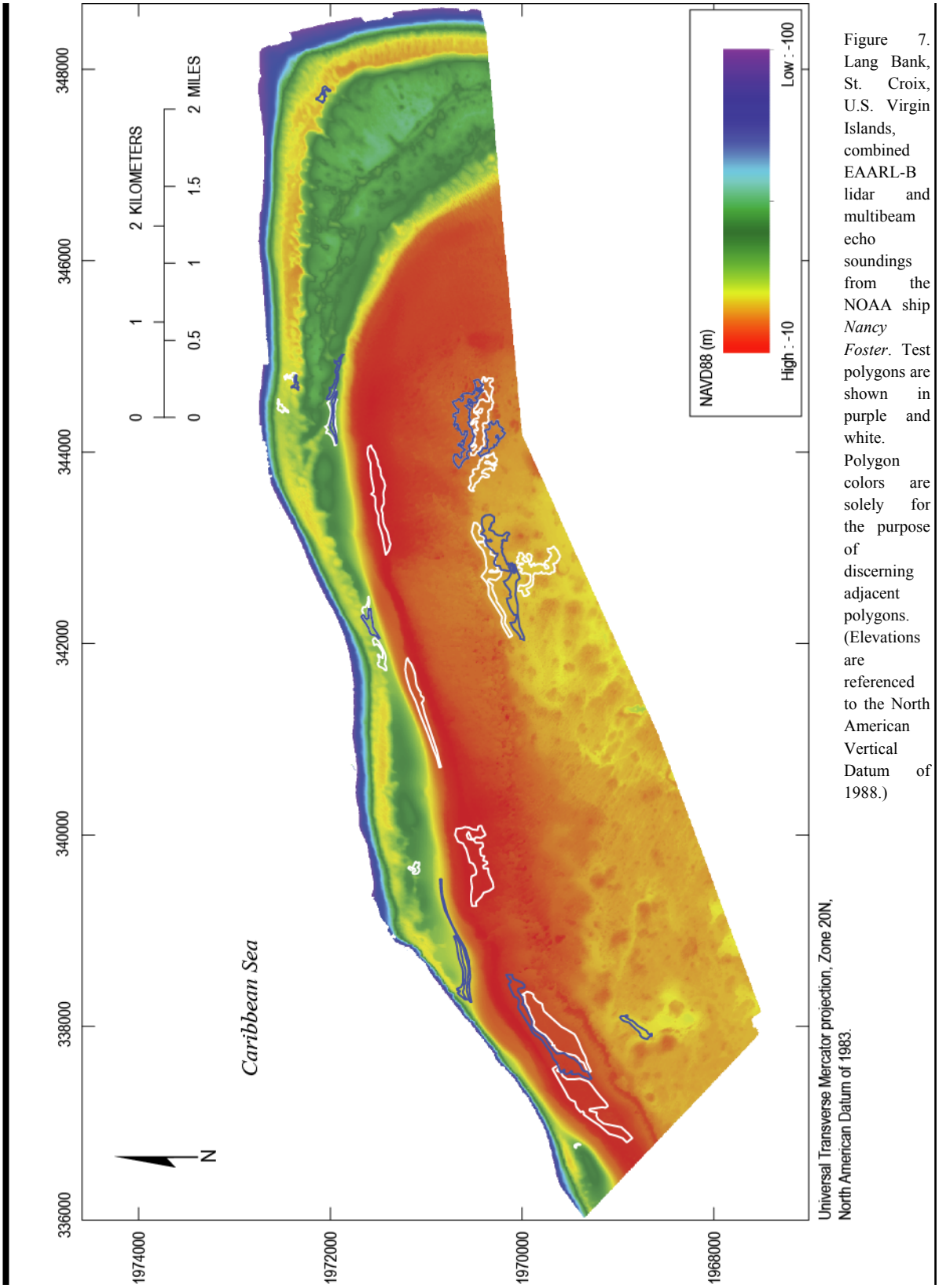

Figure 7. Lang Bank, St. Croix, U.S. Virgin Islands, combined EAARL-B lidar and multibeam echo soundings from the NOAA ship *Nancy Foster*. Test polygons are shown in purple and white. Polygon colors are solely for the purpose of discerning adjacent polygons. (Elevations are referenced to the North American Vertical Datum of 1988.)

Calibrating the SFTF EAARL-B Data

Figure 8 shows the results of the comparisons between calibrated EAARL-B and both the JALBTCX and single beam reference datasets at the SFTF site. Circles represent comparison with the JALBTCX dataset, and triangles represent comparison with the single beam jet ski data. Blue points are the mean differences between EAARL-B and the reference, and red points represent the vertical accuracy at 95% confidence. The green and dark red lines represent the IHO minimum requirements for vertical accuracy at the Special Order and Order 1 levels, respectively. Compliance with the standard is determined by the location of the red points relative to the IHO lines. If the red points fall below the green line, they satisfy the Special Order standard, whereas if they are above the green line but below the dark red line, then they only comply with the less stringent Order 1 standard.

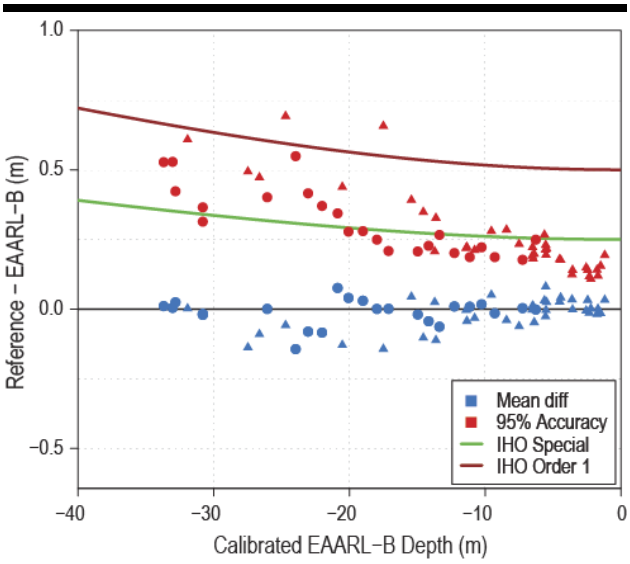

Figure 8. EAARL-B calibrated mean difference (blue) and 95% accuracy results (red) from the SFTF site. Circles are referenced to the JALBTCX dataset, and triangles are referenced to jet ski data plotted with the IHO Special Order (green) and IHO Order 1 (red line) minimum requirements for depth accuracy. The EAARL-B exceeds the Special Order down to 20 m, and Order 1 down to beyond 33 m.

The results show that the relative vertical accuracy of the EAARL-B (to the JALBTCX reference data) is within the IHO Special Order down to approximately 20-m depth and Order 1 specification for the entire depth range collected during the SFTF survey. Vertical accuracy relative to the single beam jet ski data is mostly within the IHO Special Order spec down to approximately 13 m, after which vertical accuracy decreases rapidly and nonlinearly. This is where the lack of an attitude and orientation system aboard the jet skis begins to make a significant difference. For this reason, single beam reference data at depths greater than 10 m should be viewed with suspicion.

Validating the Calibration Using the St. Croix Dataset

The depth calibration constants developed from the SFTF EAARL-B survey and JALBTCX reference data were applied to an EAARL-B dataset captured in March 2014 over Lang Bank near St. Croix, U.S. Virgin Islands. The calibrated EAARL-B data were then compared to the second reference dataset, the multibeam echosounder dataset captured by the *Nancy Foster*. Figure 9 shows the results of this analysis. As before, each blue point represents the mean difference of all the points in a single selected polygon and has a corresponding red point representing the vertical accuracy at 95%. The results indicate that more than 90% of the selected depth regions exceed the IHO Special Order requirements for vertical accuracy, with an absolute deviation from the reference of less than ±12.5 cm.

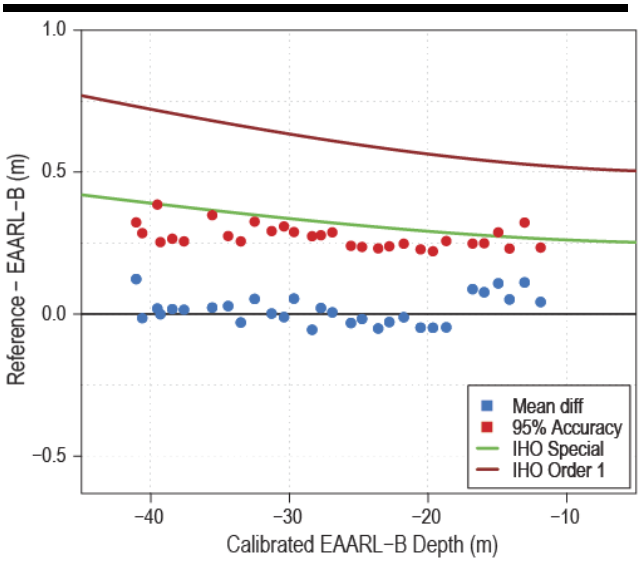

Figure 9. EAARL-B calibrated mean difference (blue) and 95% accuracy results (red dots) from the St. Croix study area plotted with the IHO Special Order (green line) and IHO Order 1 (red line) minimum requirements for depth accuracy.

Shallow-water Calibration of the Deep Channel

The purpose of this calibration effort is to determine the optimal configuration constants to range-align the large pixel receiver with the three shallow channel pixels. A series of density estimate curves like those shown in Figure 3, was plotted and the average of the differences between the pairwise means used to compute the offset that produces the best alignment.

Figure 10 shows the kernel density estimates of vertical error of raw and channel-aligned data from 12 of the 23 named regions from the SFTF site. Blue curves represent density estimates of the vertical error of uncalibrated topobathy channels and grey curves depict corresponding density estimates for uncalibrated deep-channel data. Note the increasing deviation from zero of the means of the blue and grey curves, with increasing depth. The red curves in Figure 10 show the same

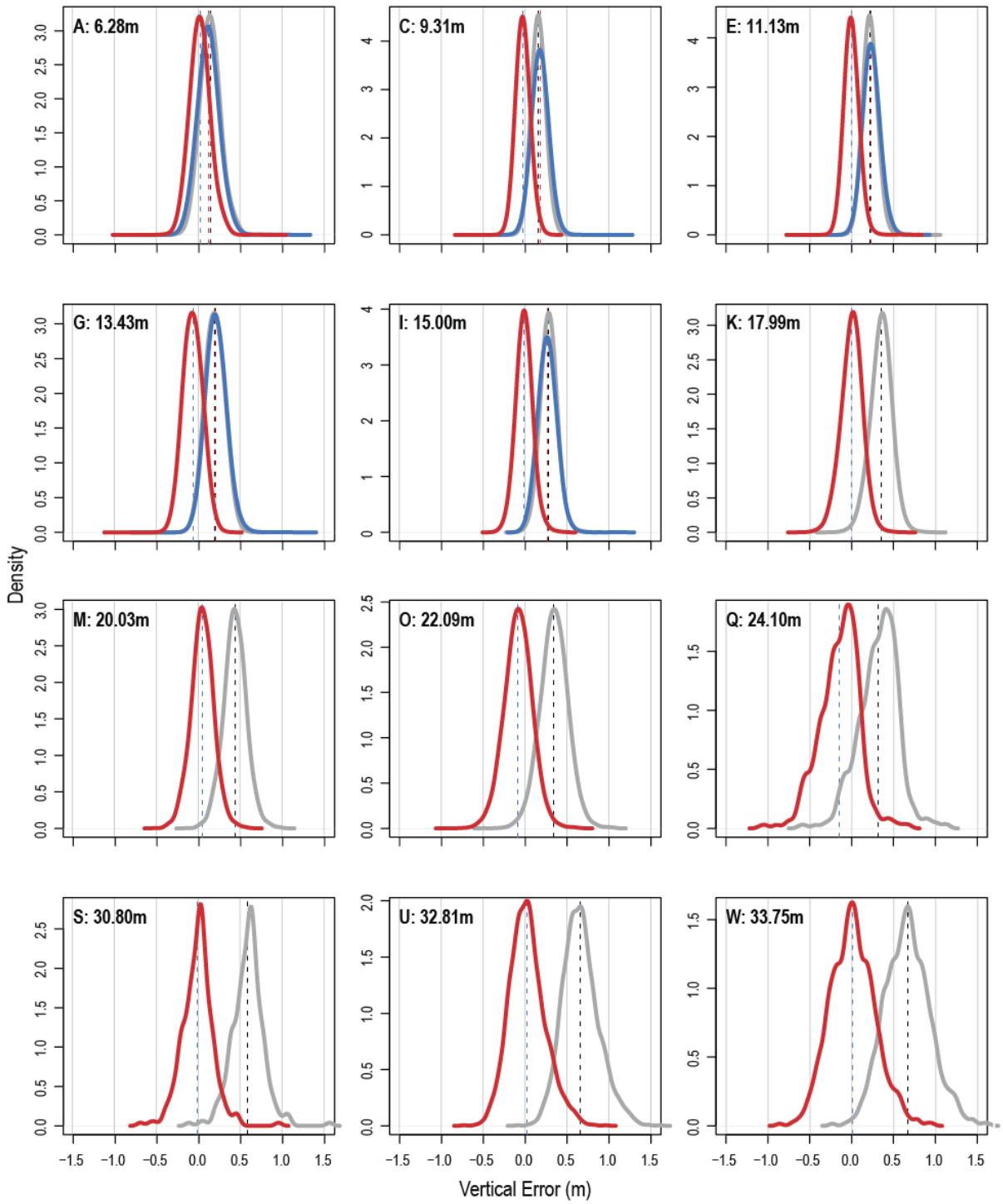

Figure 10: Kernel density estimates of vertical error for select depth regions from the SFTF survey. Blue curves represent uncalibrated EAARL-B topobathy channels, grey curves the uncalibrated deep channel, and red curves represent the calibrated deep channel. Each plot A–W was derived from data in the corresponding polygon defined in Figure 4.

distributions for deep-channel data *after* calibration. If the EAARL-B depth measurements match the reference data, the means of the density estimate curves would all be approximately zero, as is the case in the post-calibrated data (red).

The pre-calibration curves (blue and grey) indicate that uncalibrated EAARL-B data exhibit a deep bias because their means are positive and the deviation from zero increases as depth increases. Blue curves appear on only the first five plots because the shallow channels produced returns down to approximately 15 m, whereas the deep channel (red and grey) produced returns to roughly 34 m. The curves for polygons A–I also indicate excellent alignment between the topobathy channels and the deep channel.

Figure 11 shows the results of a comparison between topobathy-channel depths and deep-channel depths from the SFTF EAARL-B survey. More than 6 million point matches resulted, and their differences were binned into 1-m bins. The relation between the binned differences and the topobathy channel depth is depicted in Figure 11. The average difference is 0.9 cm with a coefficient of determination (R-squared) of greater than 99.9.

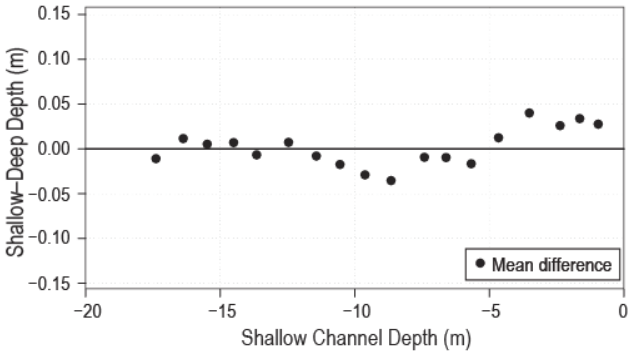

Figure 11. Comparison of deep- to shallow-channel depth measurements.

CONCLUSIONS

This extensive, empirical study provided answers to the six central questions that formed the starting point for the work. Two calibration constants were found that can be used in a simple linear equation to correct the EAARL-B depth data to agree with the reference datasets. The constants are a scale factor of 0.98103 and an offset of –0.00068 m, and were found to hold well in comparisons using different reference datasets and geographic locations. Additionally, the topobathy channels were found to track the deep channel over the entire operational depth range of the topobathy channels. This finding is important because the shallow channels operate very differently from the deep channel. The deep channel is viewing backscatter from an area that is much larger than each of the topobathy channel areas. Additionally, the deep channel is blind to the surface return and can only see scattered light from each of the shallow-channel beams.

The subsurface scatter from the three surface spots combines within the deep-channel field of view and yields a depth measurement that meets or exceeds the vertical accuracy requirements of the IHO S-44-5E Standards for Order 1 for depths from 0 to 41 m. (Again, this study only considered depth-measurement uncertainty; assessments of other components of the IHO S-44 standards were considered beyond the scope of this work.) The deep-channel depth measurements track well with the topobathy channels, and the average difference between them over the range of 1 to 16 m was 0.9 cm, with a standard deviation of 8.4 cm. This relationship was found to be stable with an R^2 value greater than 0.999.

Overall, the calibrated EAARL-B data were found to be in good agreement with the reference datasets for multiple test sites. The relationship is linear and consistent. The results of this work are expected to enable calibrated EAARL-B data to be used across a range of application areas, including benthic habitat mapping and monitoring, nautical charting, coastal change analysis, and coastal resource management.

FUTURE WORK

Future work will involve determining whether the calibration is stable over time, or, if not, at what temporal frequency the EAARL-B system needs to be recalibrated. Further investigation is also planned to derive calibration constants for non-clear-water conditions. EAARL-B data will be collected over a suitable test area during times of differing water clarity along with concurrent sea truth—field measurement of seafloor elevation, water column optical properties, and bottom reflectivity would be required. For each survey mission conducted, the procedure described herein will be performed. Ultimately, the goal is to have ALPS automatically determine the depth calibration coefficients based on the calculated optical properties of the water column.

ACKNOWLEDGMENTS

The work by C. Wayne Wright was done while serving as a Scientist Emeritus with the U.S. Geological Survey. The work performed by Christine Kranenburg of Cherokee Nation Technology Solutions, St. Petersburg, Florida, was done under contract to the U.S. Geological Survey. Any use of trade, firm, or product names is for descriptive purposes only and does not imply endorsement by the U.S. Government.

LITERATURE CITED

Baltsavias, E.P., 1999. Airborne laser scanning: Basic relations and formulas. *ISPRS Journal of Photogrammetry and Remote Sensing*, 54, 199–214.

Battista, T.A. and Stecher, M., 2014. *Descriptive Report to Accompany Hydrographic Survey H12639*. Silver Spring, Maryland: National Oceanic and Atmospheric Administration, National Ocean Service, *NOAA Descriptive Report, M-I907-NF-14*, 22p.

Bonisteel, J.M.; Nayegandhi, A.; Wright, C.W.; Brock, J.C., and Nagle, D.B., 2009. *Experimental Advanced Airborne Research Lidar (EAARL) Data Processing Manual*. *USGS Open-File Report 2009-1078*, 38p.

International Hydrographic Organization, 2008. *IHO Standards for Hydrographic Surveys: Special Publication No. 44, 5th*

ed. Monaco: International Hydrographic Bureau, 36p.

Grewal, M.S.; Andrews, A.P., and Bartone, C.G., 2013. *Global Navigation Satellite Systems, Inertial Navigation, and Integration*. Hoboken, New Jersey: Wiley, 608p.

Guenther, G.C., 1985. *Airborne laser hydrography: System design and performance factors*. Rockville, Maryland: National Oceanic and Atmospheric Administration, *NOAA Professional Paper Series, National Ocean Service 1*, 396p.

Guenther, G.C.; LaRocque, P.E., and Lillycrop, W.J., 1994. Multiple surface channels in Scanning Hydrographic Operational Airborne Lidar Survey (SHOALS) airborne lidar. *Proceedings of SPIE: Ocean Optics XII* (Bergen, Norway), pp. 422–430.

Guenther, G.C.; Thomas, R.W.L., and LaRocque, P.E., 1996. Design Considerations for Achieving High Accuracy with the SHOALS Bathymetric Lidar System. *Proceedings of SPIE 2964: Laser Remote Sensing of Natural Waters: From Theory to Practice* (St. Petersburg, Russia), pp. 54−71.

Hansen, M., 2008. SANDS: A high accuracy bathymetric survey system for shallow water mapping, *Oceanology 2008*, (London, England), poster presentation, 1p.

Hess, K.; Jeong, I., and White, S., 2013. *Revised VDatum for Eastern Florida*. Silver Spring, Maryland: National Oceanic and Atmospheric Administration, National Ocean Service, *NOAA Technical Memorandum, NOS CS 30*, 49p.

Hutton, J.; Ip, A.; Bourke, T.; Scherzinger, B.; Gopaul, N.; Canter, P.; Oveland, I., and Blankenberg, L., 2008. Tight integration of GNSS post-processed virtual reference station with inertial data for increased accuracy and productivity of airborne mapping. *International Archives of Photogrammetry, Remote Sensing and Spatial Information Sciences*, 37(B5), 829–834.

Hamamatsu Photonics K.K., 2007. *Photomultiplier Tubes, Basics and Applications (3rd ed.)*, 323p.

Irish, J.L., and Lillycrop, W.J., 1999. Scanning laser mapping of the coastal zone: the SHOALS system, *ISPRS Journal of Photogrammetry and Remote Sensing*, 54(2–3), 123–129.

Long, B., Cottin, A., and Collin, A., 2007. What Optech's Bathymetric LiDAR Sees Underwater. *Proceedings of IEEE International Geoscience and Remote Sensing Symposium, IGARSS 2007* (Barcelona, Spain), pp. 3170–3173.

Nagle, D. and Wright, C.W., 2016. *Algorithms used in the Airborne Lidar Processing System (ALPS). USGS Open-File Report 2016–1046*, 45p.

NOAA, 2012. *VDatum Manual for Development and Support of NOAA's Vertical Datum Transformation Tool, VDatum, Version 1.01*. Silver Spring, Maryland: National Oceanic and Atmospheric Administration Publication, 127p. http://www.nauticalcharts.noaa.gov/csdl/publications/Manual_2012.06.26.doc.

Silverman, B.W., 1986. *Density Estimation for Statistics and Data Analysis*. London: Chapman and Hall/CRC Press, 176p.

Wright, C.W. and Brock, J.C., 2002. EAARL: A lidar for mapping shallow coral reefs and other coastal environments. *Proceedings of the 7th International Conference on Remote Sensing for Marine and Coastal Environments* (Miami, Florida).